CHEMISTRY

Nonconfinement growth of edge-curved molecular crystals for self-focused microlasers

Baipeng Yin[1,2,3]†, Jie Liang[2,3]†, Jinjie Hao[2,3], Chenghu Dai[2], Hao Jia[2,3], Hong Wang[2,3], Desong Wang[1], Fang-Jie Shu[4], Chuang Zhang[2]*, Jianmin Gu[1]*, Yong Sheng Zhao[2,3]*

Synthesis of single-crystalline micro/nanostructures with curved shapes is essential for developing extraordinary types of optoelectronic devices. Here, we use the strategy of liquid-phase nonconfinement growth to controllably synthesize edge-curved molecular microcrystals on a large scale. By varying the molecular substituents on linear organic conjugated molecules, it is found that the steric hindrance effect could minimize the intrinsic anisotropy of molecular stacking, allowing for the exposure of high-index crystal planes. The growth rate of high-index crystal planes can be further regulated by increasing the molecular supersaturation, which is conducive to the cogrowth of these crystal planes to form continuously curved-shape microcrystals. Assisted by nonrotationally symmetric geometry and optically smooth curvature, edge-curved microcrystals can support low-threshold lasing, and self-focusing directional emission. These results contribute to gaining an insightful understanding of the design and growth of functional molecular crystals and promoting the applications of organic active materials in integrated photonic devices and circuits.

INTRODUCTION

Microdisk lasers hold great potential in applications ranging from laser display, high-throughput sensing, on-chip optical communication, to computing, owing to their planar geometry, high *Q* factors, low threshold, and in-plane light emission (*1*–*4*). Recently, the deformed microcavities with smoothly curved shapes can effectively focus the electromagnetic energy into a certain direction by breaking the rotational symmetry of microdisk lasers, which is beneficial to the controllable and high-power output of optical signals (*5*–*8*). To meet the requirements of symmetry-breaking curved structures, most of the deformed microcavities were fabricated on amorphous materials or inorganic semiconductors using high-precision etching techniques, such as photolithography and electron beam etching (*9*, *10*). Compared with traditional optical gain materials, organic microcrystals not only show excellent solution processability as well as the flexibility in molecular design but also exhibit excellent broadband gain performance due to their abundant energy levels and excited-state processes (*11*–*16*). However, due to the self-confinement nature of crystal growth, that is, crystals spontaneously grow into symmetric convex polyhedra morphologies (*17*, *18*), the synthesis method of single-crystalline curved-shape micro/nanostructures with high quality and large quantities still needs to be explored.

The shape anisotropy of crystals is mainly determined by the inherent anisotropy in the stacking arrangement and the interaction between its basic units (*19*–*21*). In general, molecular crystals have stronger anisotropy than atomic crystals in macroscopic morphology because molecular units have a more complicated structure and lower geometrical symmetry. The chemical versatility of organic materials enables the molecular design, such as the introduction of side-group alkyl chains or aromatic group, to tune the packing style through the steric effects and then change the crystal morphology (*22*–*26*). Besides, the modification of side groups may alter the weak intermolecular interaction between molecular units and provide the possibility to regulate the growth anisotropy of molecular crystals through the outer environment in the subsequent synthesis process, including solvent polarity, volatilization speed, solution concentration, etc. (*27*–*29*). In particular, the supersaturation of growth environment, which is directly related to the surface attachment energies, can effectively adjust the growth rate of crystal planes and further promote the evolution of the straight edges to smooth curved edges (*30*–*32*). The combination of rational molecular design and optimized preparation conditions would lead to the nonconfinement growth of molecular crystals, which is promising for the construction of self-assembled deformed microcavities toward low-threshold self-focused microlasers.

Here, we demonstrate a liquid-phase nonconfinement growth strategy for the fabrication of eye-shaped microcrystals on a large scale, which involves rational molecular modulation and a solvent-antisolvent synergistic effect. 4,4′-Bis[4-(di-p-tolylamino)styryl] biphenyl (DPAVBi) and 4,4′-bis[4-(diphenylamino)styryl]biphenyl (BDAVBi), two molecules with the same backbone but different substituents, are selected as model compounds owing to their outstanding excited-state gain properties. Compared with DPAVBi, the phenyl groups with a lower steric hindrance on the BDAVBi molecule can effectively avoid π-π interaction to inhibit tight anisotropic stacking in the crystals, thus promoting the appearance of more high-index crystal planes along crystal edges. Moreover, the growth rate of these crystal planes can be facilely tuned by increasing the molecular supersaturation during the liquid-phase preparation process, which is beneficial for a nonconfinement growth by forming the curved boundaries. The synthesized eye-shaped microcrystals with controlled morphological and size parameters can serve as deformed microcavities. Assisted by the asymmetric light propagation, they can support low-threshold lasing and self-focusing emission of high-*Q*

[1]State Key Laboratory of Metastable Materials Science and Technology (MMST), Yanshan University, Qinhuangdao 066004, China. [2]Key Laboratory of Photochemistry, Beijing National Laboratory for Molecular Sciences, Institute of Chemistry, Chinese Academy of Sciences, Beijing 100190, China. [3]University of Chinese Academy of Sciences, Beijing 100049, China. [4]Engineering Research Center for Photoelectric Intelligent Sensing, Department of Physics, Shangqiu Normal University, Shangqiu 476000, China.
*Corresponding author. Email: zhangc@iccas.ac.cn (C.Z.); jmgu@ysu.edu.cn (J.G.); yszhao@iccas.ac.cn (Y.S.Z.)
†These authors contributed equally to this work.

mode light. These results illustrate that the nonconfinement growth approach exhibits a deep understanding for the crystal growth and holds great potentials in the development of active nanophotonic materials and devices.

RESULTS

π-Conjugated organic molecules DPAVBi (Fig. 1A) (*33*) and BDAVBi (Fig. 1B) (*34*) are adopted to explore the influence of the molecular substituents on the curved boundaries of self-assembled microcrystals. Both molecules are stilbene derivatives; DPAVBi is modified by four tolyl groups on the molecular backbone, while BDAVBi is substituted by phenyl groups at the same position. This slight change in molecular structure may cause substantial variation in their intermolecular interactions and packing styles (*19*, *29*). To understand the relationship between molecular structure and crystal morphology, we simulate the growth morphology of DPAVBi and BDAVBi crystals based on the attachment energies. As shown in Fig. 1C, the packing styles of DPAVBi molecules adopt a triclinic crystal with high spatial asymmetry in the crystal (table S1), and its in-plane growth morphology is enclosed by (001), (010), and (011) low-index crystal planes with almost the same surface areas. In contrast, the packing styles of BDAVBi molecules adopt a monoclinic crystal (table S2) with spatial symmetry within the crystal *bc* plane. The more high-index crystal planes with different surface areas, such as (12-2) and (13-3) crystal planes, evolved between these low-index crystal planes to form the quasi-continuous side faces (Fig. 1D). Therefore, the crystal boundary clearly shows some curvature at this stage. In the experiment, DPAVBi and BDAVBi self-assembled into the microcrystals by a facile antisolvent diffusion combined with the solvent evaporation method (fig. S1) (*35*). The morphology of as-prepared DPAVBi and BDAVBi microcrystals is inconsistent with the above predicted results (Fig. 1, E and F). More impressively, the BDAVBi microcrystals exhibit a curved boundary that is notably different from the straight boundary of DPAVBi microcrystals prepared under the same experimental conditions. It implies that the phenyl groups with less steric hindrance can promote the synthesis of smooth single crystals by regulating the growth of high-index crystal planes.

To further understand the formation of the curved boundary, we investigate the growth mechanism of DPAVBi and BDAVBi microcrystals both theoretically and experimentally. In DPAVBi molecules, the tolyl group is more coplanar with the molecular backbone due to its large steric hindrance that inhibits the torsion of the molecular backbone (*36*). Therefore, DPAVBi molecules are forced into a cofacial π-stack with large intermolecular π-π orbital overlap by multiple π-π interactions and CH-π interactions (fig. S2). As a result, DPAVBi crystals show a clear crystal growth anisotropy along the direction of π-π interaction (fig. S3 and Fig. 1E). In BDAVBi molecules, the molecular backbone exhibits better flexibility due to the phenyl group having less steric hindrance, with the dihedral angles between terminal benzene rings and the central benzene ring being about 45°. The larger dihedral angle of BDAVBi molecules effectively inhibits π-π interactions between the molecules of adjacent stacks. Thus, nondirectional CH-π interactions are the predominant driving force during self-assembly (Fig. 2A), which facilitates a herringbone packing with a large intermolecular distance (fig. S4). As shown in Fig. 2B and fig. S5, the shortest distance between the neighboring parallel BDAVBi molecules (labeled as 1 and 2) is about 4.65 Å, which is much larger than that the molecular separation of DPAVBi molecules (~3.48 Å). The loosely packed structures of BDAVBi molecules can break the in-plane growth anisotropy and permit the exposure of high-index crystal planes along the edges of the BDAVBi microcrystal, as revealed by the two-dimensional x-ray diffraction (2D-XRD) measurement (fig. S6) (*17*, *21*). Hence, the molecular flexibility and the steric hindrance may play a decisive role in the loosely packing styles of linear organic conjugated molecules, which then provide the possibility for the regulation of smoothly curved boundary during the crystal growth process.

The shape of crystals is not only related to the building blocks but also governed by the chemical environment in liquid phase. Therefore,

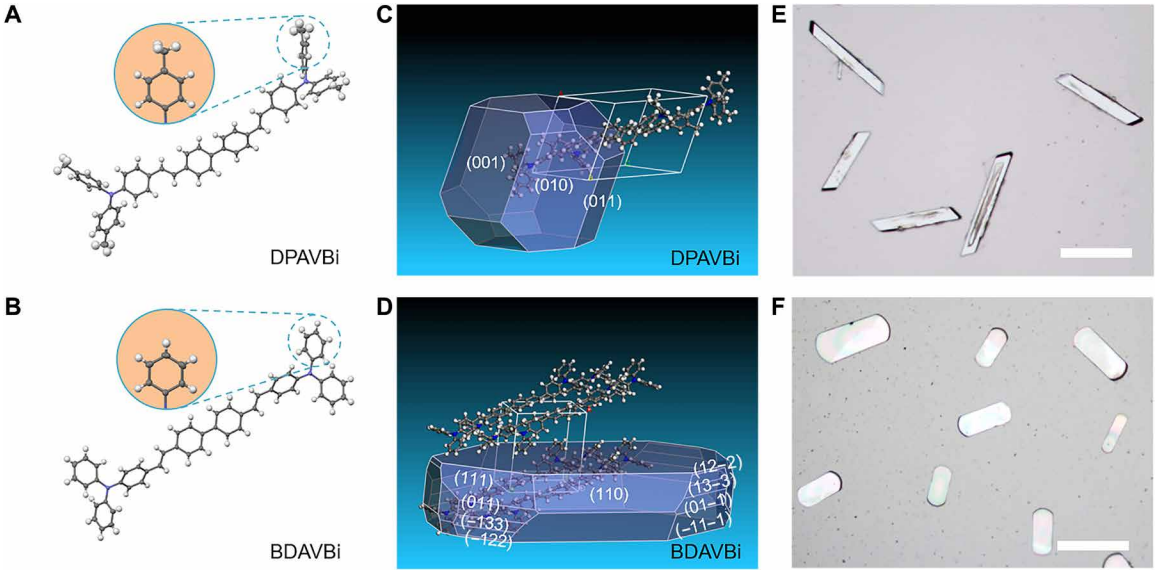

Fig. 1. Rational molecular modulation. Molecular structures of (**A**) DPAVBi and (**B**) BDAVBi. The simulated growth morphology of (**C**) DPAVBi microcrystals and (**D**) BDAVBi microcrystals based on attachment energy. Optical microscopy images of (**E**) DPAVBi microcrystals and (**F**) BDAVBi microcrystals. Scale bars, 20 μm.

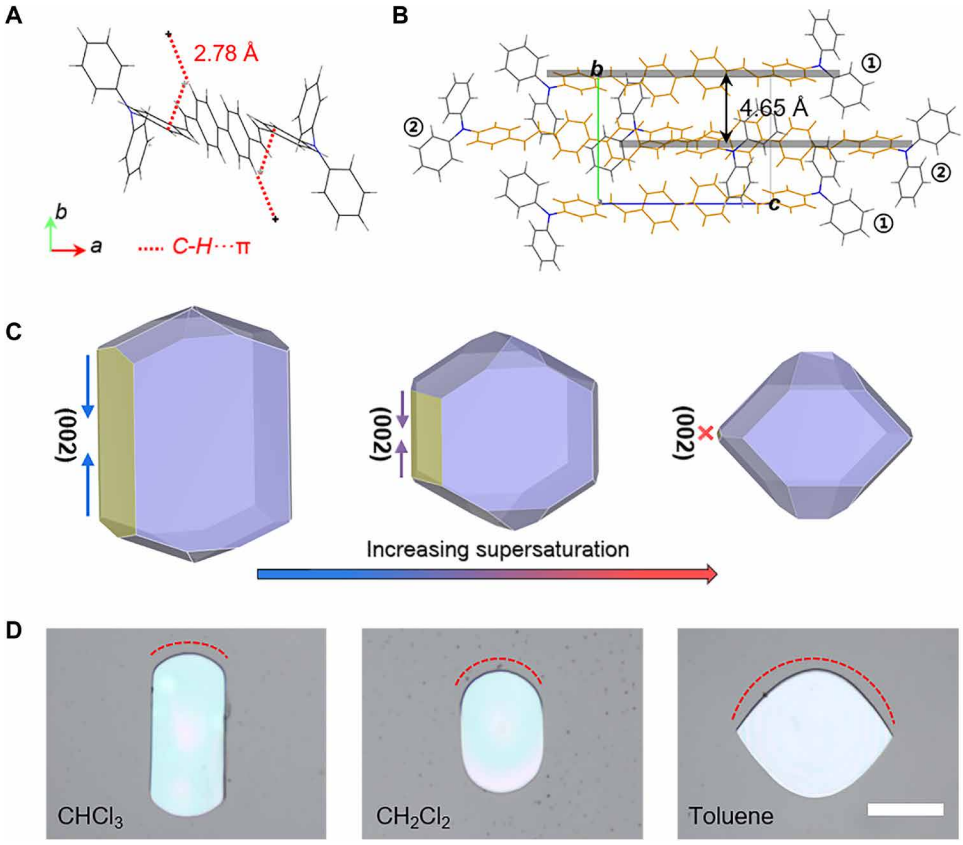

Fig. 2. Solvent-antisolvent synergistic effect. (**A**) Intermolecular interactions measured in eye-shaped BDAVBi microcrystals. (**B**) Molecular arrangement viewed perpendicular to the top face of eye-shaped BDAVBi microcrystals. (**C**) Morphological evolution of BDAVBi crystals predicted by molecular dynamics simulation based on the interaction between crystals and antisolvents. (**D**) Optical microscopy images of BDAVBi microcrystals grown using different antisolvents. Scale bar, 15 μm.

the molecular dynamics simulation (Fig. 2C) is performed on the morphologies of BDAVBi crystals on the basis of their interactions with solvents. When the polarity of solvent gradually increases, the growth on crystal plane (002) (corresponding to straight boundary, fig. S7) is prohibited; thus, the ratio between curved and straight boundaries increases in BDAVBi microcrystals. The side faces of the BDAVBi crystal are composed of the high-index crystal planes with high growth barrier (Fig. 1D); hence, the antisolvent-induced supersaturation change also further regulates the curvature of the curved boundary (dashed red line in Fig. 2D) (*32*). The supersaturation of BDAVBi gradually increases with the polarity of antisolvents ($CHCl_3$: polarity index 4.2, CH_2Cl_2: polarity index 3.4, and toluene: polarity index 2.4), thus providing a sufficiently high chemical potential (Δμ) to overcome the growth barrier of high-index crystal planes (*31*). Therefore, more crystal planes (table S3) are exposed along the crystal edges. The cogrowth of these crystal planes eventually forms a curved-edge microcrystals with dynamically stable morphology and exhibits good curved-edge adjustable characteristics. By changing the antisolvents in the preparation process, the aspect ratio of DPAVBi microrods gradually decreases, but no well-curved crystals can be observed even at high supersaturation (fig. S8). The above results indicate that the rationally designed solvent-antisolvent synergistic effect is an essential factor for the nonconfinement growth of BDAVBi crystals by forming numerous high-index crystal planes.

By optimizing the nonconfinement growth process, the eye-shaped BDAVBi microcrystals have well-defined curved boundaries and flat outer surfaces, as shown in the scanning electron microscopy (SEM) image (Fig. 3A). The distribution diagram of the size parameter (*L*, long axis) and the morphological parameter (*L*/*S*, long axis/short axis) indicates the high uniformity of these synthesized eye-shaped microcrystals using a liquid-phase growth strategy (fig. S9). Transmission electron microscopy (TEM) image and the selected-area electron diffraction (SAED) patterns obtained from different regions reveal the single-crystal nature of whole eye-shaped microcrystals (Fig. 3B). It should be noted that the curved edge consists of many tiny crystal facets at the microscopic scale (fig. S10). According to single-crystal XRD data, the growth directions of eye-shaped microcrystals are parallel to the substrate, which are ascribed to the [110] and [011] of the monoclinic structure, respectively. It is further found that only a series of peaks corresponding to the (100) crystal plane appears in the XRD spectrum, such as (200), (300), (400), and (500) peaks, indicating that eye-shaped microcrystals adopt a lamellar structure with the (100) crystal plane parallel to the substrate (fig. S11). The high-crystallinity nature and highly smooth surfaces of eye-shaped microcrystals would minimize the optical propagation loss, which are essential for effective propagation of the photoluminescence (PL) energy.

As shown in Fig. 3C, eye-shaped microcrystals exhibit strong green fluorescence with typical features of active optical waveguides

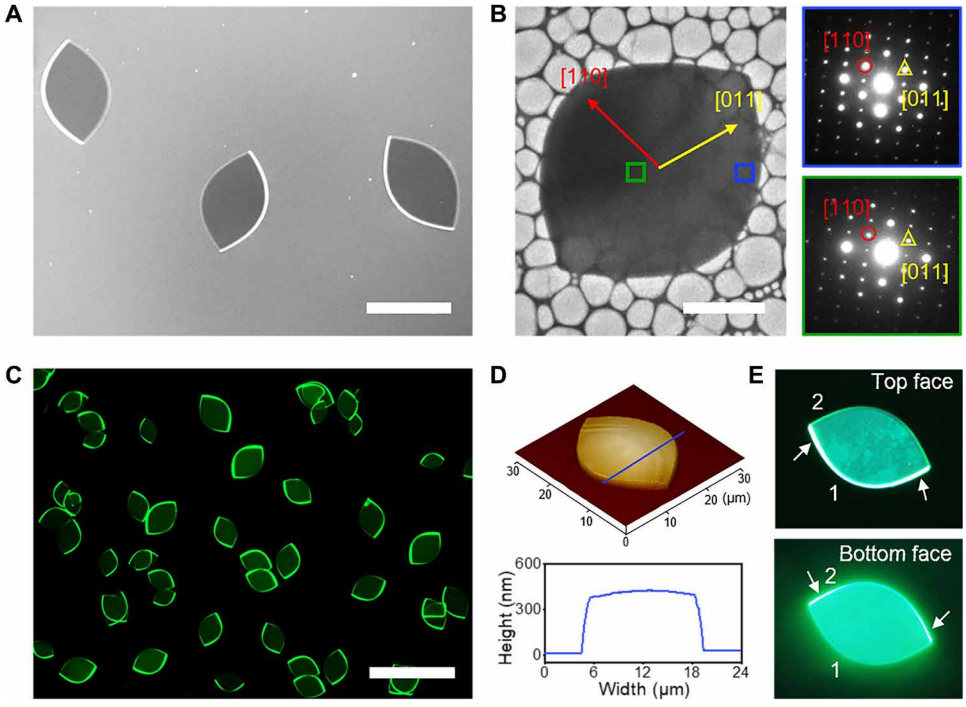

Fig. 3. Preparation of eye-shaped microcrystals. (**A**) SEM image of eye-shaped microcrystals. Scale bar, 20 μm. (**B**) TEM image and SAED patterns of a single eye-shaped microcrystal. Scale bar, 10 μm. (**C**) Fluorescence microscopy image of eye-shaped microcrystals. Scale bar, 50 μm. (**D**) AFM topography and height diagram of an eye-shaped microcrystal. (**E**) Fluorescence microscopy images from the top face and bottom face of an eye-shaped microcrystal.

under the excitation of unfocused ultraviolet light (330 to 380 nm). All eye-shaped microcrystals show strong emission from one curved boundary, which shows significant contrast with weak emission from the opposite curved boundary. The atomic force microscopy (AFM) image shows that there is a symmetrical cross section of ~400-nm thickness in the short axis of eye-shaped microcrystals, which excludes the contribution of the geometric structure on the *z*-axis direction to the asymmetric optical waveguide (Fig. 3D). To determine the mechanism of the asymmetry optical waveguide, we collected fluorescence microscopy images of the top face and bottom face of eye-shaped microcrystals (Fig. 3E). The position of strong emission changes from the curved boundary 1 viewed from the top face to the curved boundary 2 viewed from the bottom face, which indicates that the asymmetry optical waveguide in the crystals may be related to the molecular arrangement. In eye-shaped microcrystals, the transition dipole of the BDAVBi molecule is along the molecular long axis (*37*), while the molecular long axis is tilted at an angle of 23° with respect to the upper surface of eye-shaped microcrystals (fig. S12). Therefore, the emitted light of BDAVBi was guided mainly within a plane perpendicular to the molecular long axis, that is, tilted with respect to the upper surface of eye-shaped microcrystals.

BDAVBi is a typical intramolecular charge-transfer (ICT) compound, as indicated by the DFT calculation and solvent polarity-dependent emission spectra (fig. S13). Because of the photophysical properties of the ICT excited state, the BDAVBi microcrystals exhibit outstanding optical properties with a solid quantum yield φ of ~33% and efficient radiative decay rate $k = 6.22 \times 10^8$ s^{-1} according to the equation, $k = \varphi/\tau$ ($\tau = 0.49$ ns; fig. S14). The quantum yields for stadium-shaped and eye-shaped microcrystals are almost the same as they share the same molecular packing mode, and thus, it allows us to study the influence of microcavity boundaries on the laser performance of BDAVBi microcrystals. These excellent optical properties together with the unique optical cavity geometry make eye-shaped microcrystals a candidate for supporting self-focusing emission of high-*Q* mode laser. The lasing action in eye-shaped microcavity was investigated using a microphotoluminescence setup equipped with a pulsed laser (400 nm, 200 fs, 1 kHz) (fig. S15). Figure 4A shows the PL image and corresponding emission spectra of a single eye-shaped microcavity with geometry parameters of $L = 20$ μm and $L/S = 1.6$ excited with gradually increasing pump energy. At a low pump energy (2.16 μJ cm^{-2}), the broad spontaneous emission from eye-shaped microcavity centered at 495 nm was observed. As the pump energy increased, discrete sharp peaks appeared on top of the broad emission band, and their intensity rapidly increased in the emission spectra, which is indicative of the occurrence of optically pumped lasing. The full width at half maximum at 495 nm markedly narrows down to ~0.17 nm when the pump energy reaches 2.16 μJ cm^{-2}, revealing a significant increase in temporal coherence (fig. S16). Compared with eye-shaped microcrystals, the stadium-shaped BDAVBi microcrystals show a lasing action only when the pump energy exceeds 6.68 μJ cm^{-2} (Fig. 4B). It indicates that the curved boundaries created by the nonconfinement growth of eye-shaped microcrystals can effectively reduce optical loss. Thus, the eye-shaped microlaser exhibits a very low threshold of ~2.80 μJ cm^{-2} that is notably lower than that of the stadium-shaped microlaser (Fig. 4C). In addition, we collected the pump energy–dependent emission spectra of eye-shaped microcavity with different *L*/*S* values, and all the samples showed obviously nonlinear light amplification behavior, which verified the robust lasing performance of various eye-shaped microcrystals (fig. S17).

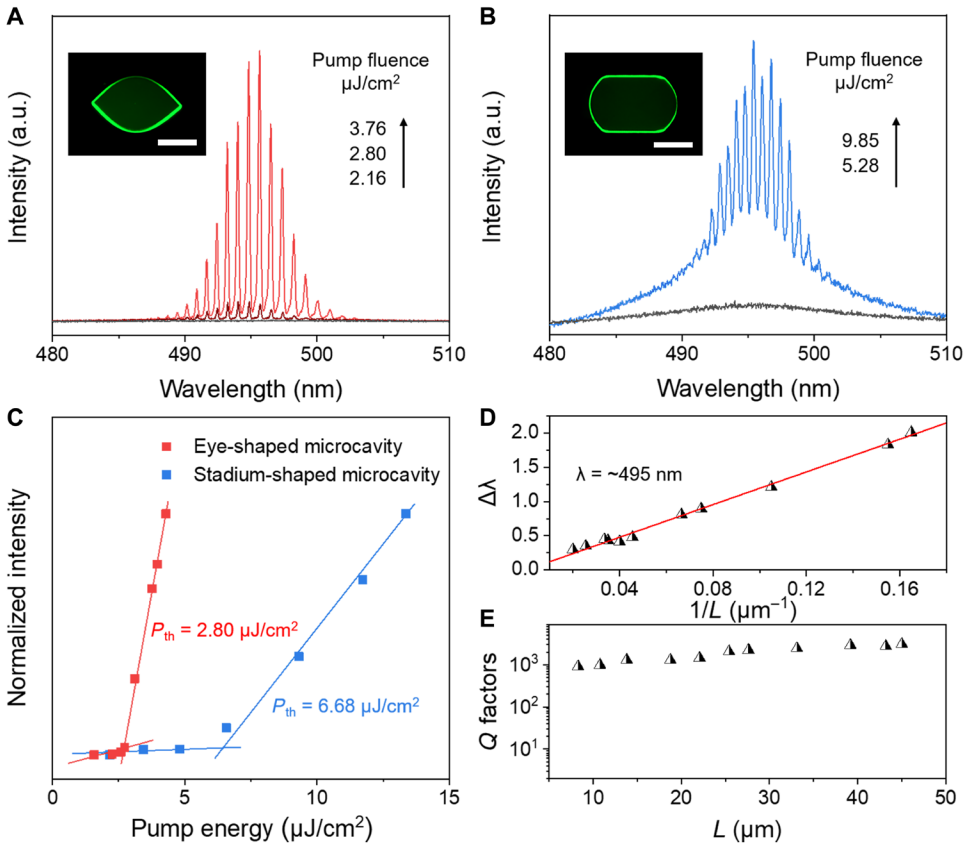

Fig. 4. Low-threshold lasing. (**A**) Emission spectra of eye-shaped microcrystals as a function of pump energy. Inset: Corresponding PL image. Scale bar, 10 μm. a.u., arbitrary units. (**B**) Emission spectra of stadium-shaped microcrystals as a function of pump energy. Inset: Corresponding PL image. Scale bar, 10 μm. (**C**) PL intensity of eye-shaped (red squares) and stadium-shaped microcrystals (blue squares) around the mode peak 495 nm as a function of pump energy. (**D**) Plot and fitted curve of mode spacing around the mode peak 495 nm versus reciprocal of *L* value. (**E**) *Q* factors of eye-shaped microcrystals with various *L* values.

To evaluate the contribution of the curved boundaries of the eye-shaped microcavity to the low-threshold laser, we collected the lasing spectra of eye-shaped microcrystals with the same morphological parameters (L/S = 1.6) but different size parameters (fig. S18). The well-fitted linear relationship between the lasing mode spacing ($\Delta\lambda$) and the reciprocal of L confirms that the curved eye-shaped microcavity is very similar to the whispering gallery mode (WGM) microcavity in which the laser resonance orbit is limited near to the boundaries (Fig. 4D) (*18*). The condition of total internal reflection for the light propagation is still valid due to the optically smooth curvature of the eye-shaped microcavity; thus, the light trajectory is highly localized and the *Q* factor of the eye-shaped cavity can be up to 3×10^3 (Fig. 4E). Besides, the laser spectrum collected from the eye-shaped microcavity with damaged boundary shows very irregular optical modes, which further confirms this conclusion (fig. S19). Therefore, the confinement effect of the eye-shaped microcavity on the light is not weakened, and the high-*Q* value of the WGM resonator is maintained. These features are favorable to the lasing performance of BDAVBi eye-shaped microcrystals compared to previously reported optically pumped lasing from stilbene derivatives (table S4) (*36*, *38*, *39*).

In addition to their low-threshold laser characteristics, the eye-shaped microcavity supports self-focused directional emission owing to its nonrotationally symmetric geometry. As shown in Fig. 5A, a BDAVBi eye-shaped microcrystal with L/S = 3 is selected to investigate the directional light outcoupling characteristics from deformed microcavities. Simulated electric field distribution of eye-shaped microcavity shows that the light energy localized at the boundary escapes rapidly at the leaky region near the tips, which implies a strong emission maximum in the normal direction of the points of maximum curvature in the far field (Fig. 5B). Although the eye-shaped microcavity allows for chaotic ray dynamics, the directional light outcoupling is mainly determined by the WGM-like stable periodic orbit (fig. S20) (*40*–*44*). To verify our above hypothesis about the self-focusing emission behavior, we collect the far-field emission of the laser by fixing the microcrystals on a rotating mount (angle change in the x-y plane is defined as θ with respect to the y axis). As shown in Fig. 5C, under the excitation of the laser beam, a bright light beam is outcoupled anisotropically from the left (*L*) side of the top face that is stronger than the right (*R*) side. In the corresponding far-field emission pattern (Fig. 5D), it is found that the laser generated in the eye-shaped microcavity, mainly emission in two directions from the unilateral boundary on the cavity, shows a highly self-focusing emission behavior with a divergence angle of less than 20°. Furthermore, the comparison of the far-field emission from the individual lasing mode shows that all lasing modes have the same output direction and similar divergence angle (fig. S21).

The PL images and far-field emission patterns collected from the top face and bottom face of the eye-shaped microcavity show that

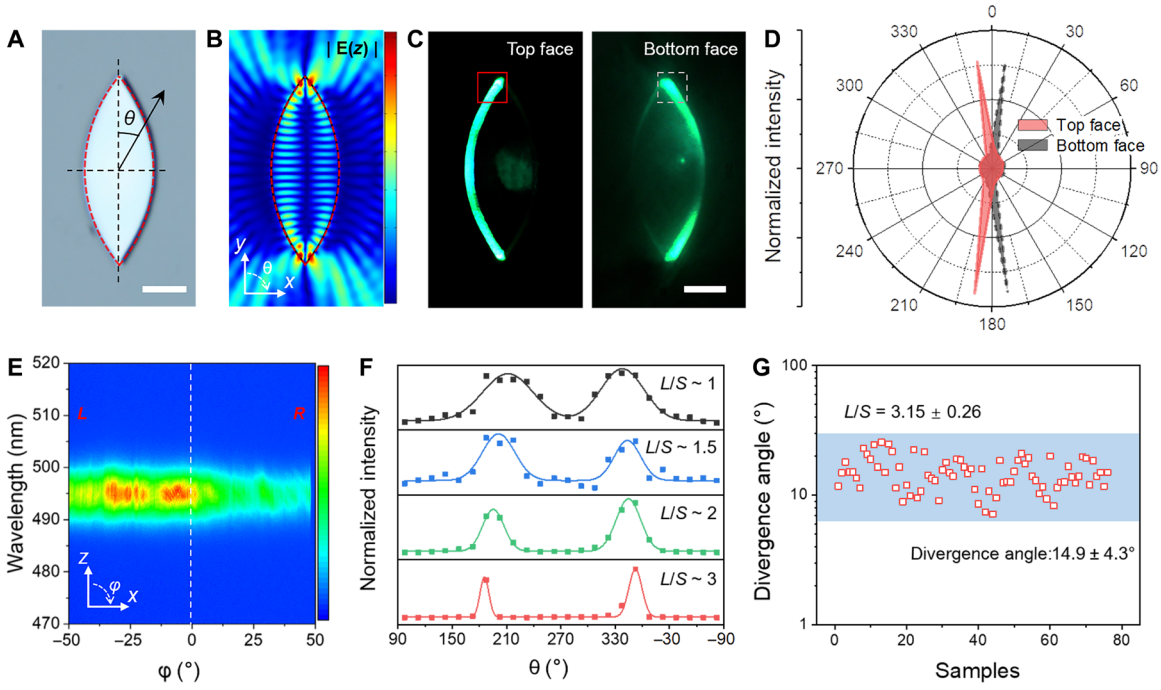

Fig. 5. Self-focused directional emission. (**A**) Optical microscopy image of the eye-shaped microcrystal with $L/S = 3$. (**B**) Simulated electric field distribution in the eye-shaped microcavity with $L/S = 3$ in the x-y plane. The dashed red curves in (A) and (B) indicate the same boundaries. (**C**) PL images from the top face and bottom face of the eye-shaped microcrystal excited uniformly with a pulsed laser. Scale bar, 5 μm. (**D**) Far-field emission pattern from the top face and bottom face of the eye-shaped microcavity with $L/S = 3$. (**E**) Angle-resolved PL spectrum of the eye-shaped microcavity. Excitation wavelength is 400 nm. (**F**) Far-field emission patterns of eye-shaped microcavities with various L/S values fitted by the Lorentzian function. (**G**) Laser divergence angle from eye-shaped microcavities with a similar L/S value of ~3.

the outcoupled light beam at the curved boundaries is focused and emitted in opposite directions under the guidance of the asymmetric light propagation. We refer to this phenomenon as the self-focusing directional emission from the eye-shaped microcavity, which is consistent with the result of the angular resolution spectrum in the x-z plane (angle change in the x-z plane is defined as φ with respect to the z axis; Fig. 5E). As shown in fig. S22, the eye-shaped microcavity exhibits a good mode modulation capability with the change of the L/S value, while its high-Q characteristics do not change significantly. The laser divergence angle and the emission angle of the eye-shaped microcavity decrease when the L/S value increases (Fig. 5F), and the trend is in agreement with the simulation result (fig. S23). It shows that reasonable cavity design is effective to improve cavity mode characteristics and self-focusing emission behavior. By designing the shape of the eye-shaped microcavity appropriately, we find that the curvature of eye-shaped microcrystals in the range of L/S = 2.0 to 3.0 is optimal for self-focused microlasers considering both lasing threshold and divergence angle (fig. S24). We have measured the far-field emission patterns of ~80 crystals with similar L/S values (3.15 ± 0.26). As shown in Fig. 5G, nearly all of these eye-shaped microcrystals show a small divergence angle of 14.9° ± 4.3° for lasing outcoupling. It proves the robustness and reproducibility of the self-focused microlasers based on BDAVBi eye-shaped microcrystals. The nonconfinement growth method could be applied to a variety of organic optical gain materials with high quantum yields (e.g., aggregation-induced emission compounds) for potential applications in integrated photonics (*45*–*47*).

DISCUSSION

In summary, we have demonstrated a liquid-phase nonconfinement growth method for the large-area construction of curved organic microcrystals. The CH-π interaction has been proven to be the driving force to form a loose packing style of the BDAVBi molecule, which can break the in-plane growth anisotropy and permit the exposure of more high-index crystal planes along microcrystal edges. Increasing the supersaturation of the BDAVBi solution can further regulate the growth rate of high-index crystal planes, which is conducive to the cogrowth of these crystal planes to form continuously curved-shape microcrystals. The structure asymmetry introduces chaotic modes in addition to the WGM resonance, which guides the light in the eye-shaped microcavity with a chaotic trajectory. Therefore, they show low-threshold lasing (~2.80 μJ cm^{-2}) and self-focusing emission of high-Q mode light. All lasing modes from eye-shaped microcrystals have the same output direction with a tunable divergence angle down to ~20°. The proposed nonconfinement growth strategy has the potential to provide an improved method with respect to the existing techniques for controllable preparation of novel photonic materials with curved shapes.

MATERIALS AND METHODS

Materials

BDAVBi (99%) was purchased from Nichem (Taiwan, China). DPAVBi (99%) was purchased from Macklin (Shanghai, China). All chemicals were purchased from InnoChem (Beijing, China) and used without further purification.

Preparation of eye-shaped microcrystals

Eye-shaped BDAVBi microcrystals were prepared through an antisolvent diffusion-combined solvent evaporation-induced self-assembly method. In a typical preparation, 20 μl of BDAVBi/CH_2Cl_2 stock solution (1 to 5 mg ml^{-1}) was dropped onto the quartz substrate in a beaker containing 0.1 to 1 ml of antisolvent. The quartz substrate was previously cleaned by sequential ultrasonic rinses in ethanol and deionized water. To avoid direct contact between the stock solution and antisolvent, the substrate was placed on top of an inner pillar taller than the level of antisolvent. The beaker was then capped to maintain solution under a constant vapor pressure of the antisolvent to induce BDAVBi molecules to crystallize into eye-shaped microcrystals. The aspect ratio of eye-shaped microcrystals was controlled by modulating the concentration of the BDAVBi/CH_2Cl_2 solution. The size of eye-shaped microcrystals was controlled by modulating the volume of the antisolvent. The same synthetic process was also used for the preparation of DPAVBi microcrystals.

Characterization

The morphology of as-prepared organic microcrystals was examined by SEM (Hitachi, S-4800), TEM (JEOL JEM-1011), and AFM (Bruker Multimode 8). The crystal structure of organic microcrystals was examined through SAED (JEOL JEM-1011) and XRD (PANalytical Empyrean). Two-dimensional XRD measurements were performed on the Rigaku SmartLab (9 kW). Single-crystal x-ray analysis was performed on the Rigaku Saturn 724 diffractometer on a rotating anode (Mo-K radiation, 0.71073 Å). The structure was solved by the direct method using SHELXS-97 and refined with Olex2.

Optical measurements

The optical microscopy image and fluorescence microscopy image were taken on a fluorescence microscope (Nikon LV-IM) by exciting the samples with halogen and mercury lamps, respectively. The fluorescence and absorption spectra were measured using a fluorescence spectrometer (Hitachi F-7000) and an ultraviolet-visible spectrometer (Hitachi U-3010), respectively. The PL quantum yields were measured by using an absolute quantum yield spectrometer (Hamamatsu, C11347). The optical measurements on the organic microcrystals were carried out on a far-field microphotoluminescence system, equipped with a mode-locked Ti:sapphire laser, a microscope, a charge-coupled device camera, and a spectrophotometer (fig. S15). The organic microcrystals were excited with a focused 400-nm femtosecond laser (200 fs, 1 kHz), which was generated from the second harmonic emission of the fundamental output of a regenerative amplifier (Solstice, Spectra-Physics; 800 nm). The angle-resolved PL spectrum was measured on an angle-resolved microphotoluminescence (ARM) system (Ideaoptics Instruments), equipped with a solid-state laser and a fiber spectrometer.

Simulations and calculations

The growth morphologies of the organic crystals were simulated on the basis of attachment energy using the Materials Studio package. Morphological evolution of crystals was predicted by molecular dynamics simulation on the basis of the interaction between crystals and antisolvents. The electric field intensity distribution in the eye-shaped microcavity was calculated with the finite element method using COMSOL Multiphysics.

SUPPLEMENTARY MATERIALS

Supplementary material for this article is available at https://science.org/doi/10.1126/sciadv.abn8106

REFERENCES AND NOTES

1. K. J. Vahala, Optical microcavities. *Nature* **424**, 839–846 (2003).
2. W. Zhang, J. Yao, Y. S. Zhao, Organic micro/nanoscale lasers. *Acc. Chem. Res.* **49**, 1691–1700 (2016).
3. S. L. McCall, A. F. J. Levi, R. E. Slusher, S. J. Pearton, R. A. Logan, Whispering-gallery mode microdisk lasers. *Appl. Phys. Lett.* **60**, 289–291 (1992).
4. Q. Zhang, G. Li, X. Liu, F. Qian, Y. Li, T. C. Sum, C. M. Lieber, Q. Xiong, A room temperature low-threshold ultraviolet plasmonic nanolaser. *Nat. Commun.* **5**, 4953 (2014).
5. C. Liu, A. Di Falco, D. Molinari, Y. Khan, B. S. Ooi, T. F. Krauss, A. Fratalocchi, Enhanced energy storage in chaotic optical resonators. *Nat. Photonics* **7**, 473–478 (2013).
6. X. F. Jiang, Y. F. Xiao, C. L. Zou, L. He, C. H. Dong, B. B. Li, Y. Li, F. W. Sun, L. Yang, Q. Gong, Highly unidirectional emission and ultralow-threshold lasing from on-chip ultrahigh-Q microcavities. *Adv. Mater.* **24**, OP260–OP264 (2012).
7. Q. Song, L. Ge, B. Redding, H. Cao, Channeling chaotic rays into waveguides for efficient collection of microcavity emission. *Phys. Rev. Lett.* **108**, 243902 (2012).
8. F.-J. Shu, C.-L. Zou, F.-W. Sun, Y.-F. Xiao, Mechanism of directional emission from a peanut-shaped microcavity. *Phys. Rev. A* **83**, 053835 (2011).
9. J. Wang, M. Tang, Y. D. Yang, Y. Yin, Y. Chen, C. N. Saggau, M. Zhu, X. Yuan, D. Karnaushenko, Y. Z. Huang, L. Ma, O. G. Schmidt, Steering directional light emission and mode chirality through postshaping of cavity geometry. *Laser Photonics Rev.* **14**, 2000118 (2020).
10. B. Redding, A. Cerjan, X. Huang, M. L. Lee, A. D. Stone, M. A. Choma, H. Cao, Low spatial coherence electrically pumped semiconductor laser for speckle-free full-field imaging. *Proc. Natl. Acad. Sci. U.S.A.* **112**, 1304–1309 (2015).
11. J. Feng, W. Wen, X. Wei, X. Jiang, M. Cao, X. Wang, X. Zhang, L. Jiang, Y. Wu, Random organic nanolaser arrays for cryptographic primitives. *Adv. Mater.* **31**, 1807880 (2019).
12. S. Cai, H. Ma, H. Shi, H. Wang, X. Wang, L. Xiao, W. Ye, K. Huang, X. Cao, N. Gan, C. Ma, M. Gu, L. Song, H. Xu, Y. Tao, C. Zhang, W. Yao, Z. An, W. Huang, Enabling long-lived organic room temperature phosphorescence in polymers by subunit interlocking. *Nat. Commun.* **10**, 4247 (2019).
13. L. Sun, W. Zhu, W. Wang, F. Yang, C. Zhang, S. Wang, X. Zhang, R. Li, H. Dong, W. Hu, Intermolecular charge-transfer interactions facilitate two-photon absorption in styrylpyridine-tetracyanobenzene cocrystals. *Angew. Chem. Int. Ed.* **56**, 7831–7835 (2017).
14. J. H. Dou, Z. A. Yu, J. Zhang, Y. Q. Zheng, Z. F. Yao, Z. Tu, X. Wang, S. Huang, C. Liu, J. Sun, Y. Yi, X. Cao, Y. Gao, J. Y. Wang, J. Pei, Organic semiconducting alloys with tunable energy levels. *J. Am. Chem. Soc.* **141**, 6561–6568 (2019).
15. C. Zhang, C.-L. Zou, Y. Zhao, C.-H. Dong, C. Wei, H. Wang, Y. Liu, G.-C. Guo, J. Yao, Y. S. Zhao, Organic printed photonics: From microring lasers to integrated circuits. *Sci. Adv.* **1**, e1500257 (2015).
16. F. F. Xu, Y. J. Li, Y. Lv, H. Dong, X. Lin, K. Wang, J. Yao, Y. S. Zhao, Flat-panel laser displays based on liquid crystal microlaser arrays. *CCS Chem.* **2**, 369–375 (2020).
17. S. Yang, B. X. Yang, L. Wu, Y. H. Li, P. Liu, H. Zhao, Y. Y. Yu, X. Q. Gong, H. G. Yang, Titania single crystals with a curved surface. *Nat. Commun.* **5**, 5355 (2014).
18. H. Dong, C. Zhang, F. J. Shu, C. L. Zou, Y. Yan, J. Yao, Y. S. Zhao, Superkinetic growth of oval organic semiconductor microcrystals for chaotic lasing. *Adv. Mater.* **33**, e2100484 (2021).
19. K. Iwai, H. Yamagishi, C. Herzberger, Y. Sato, H. Tsuji, K. Albrecht, K. Yamamoto, F. Sasaki, H. Sato, A. Asaithambi, A. Lorke, Y. Yamamoto, Single-crystalline optical microcavities from luminescent dendrimers. *Angew. Chem. Int. Ed.* **59**, 12674–12679 (2020).
20. Y. Wang, J. Liu, H. D. Tran, M. Mecklenburg, X. N. Guan, A. Z. Stieg, B. C. Regan, D. C. Martin, R. B. Kaner, Morphological and dimensional control via hierarchical assembly of doped oligoaniline single crystals. *J. Am. Chem. Soc.* **134**, 9251–9262 (2012).
21. S. Yagai, Y. Goto, X. Lin, T. Karatsu, A. Kitamura, D. Kuzuhara, H. Yamada, Y. Kikkawa, A. Saeki, S. Seki, Self-organization of hydrogen-bonding naphthalene chromophores into J-type nanorings and H-type nanorods: Impact of regioisomerism. *Angew. Chem. Int. Ed.* **51**, 6643–6647 (2012).
22. X. Wang, H. Li, Y. Wu, Z. Xu, H. Fu, Tunable morphology of the self-assembled organic microcrystals for the efficient laser optical resonator by molecular modulation. *J. Am. Chem. Soc.* **136**, 16602–16608 (2014).
23. C. Qiu, Y. Gong, Y. Guo, C. Zhang, P. Wang, J. Zhao, Y. Che, Sensitive fluorescence detection of phthalates by suppressing the intramolecular motion of nitrophenyl groups in porous crystalline ribbons. *Anal. Chem.* **91**, 13355–13359 (2019).
24. W. Yao, Y. Yan, L. Xue, C. Zhang, G. Li, Q. Zheng, Y. S. Zhao, H. Jiang, J. Yao, Controlling the structures and photonic properties of organic nanomaterials by molecular design. *Angew. Chem. Int. Ed.* **52**, 8713–8717 (2013).
25. Y. Sun, Y. Lei, W. Hu, W. Y. Wong, Epitaxial growth of nanorod meshes from luminescent organic cocrystals via crystal transformation. *J. Am. Chem. Soc.* **142**, 7265–7269 (2020).
26. C. Qiao, C. Zhang, Z. Zhou, J. Yao, Y. S. Zhao, An optically reconfigurable Förster resonance energy transfer process for broadband switchable organic single-mode microlasers. *CCS Chem.* **4**, 250–258 (2022).

27. S. Piana, M. Reyhani, J. D. Gale, Simulating micrometre-scale crystal growth from solution. *Nature* **438**, 70–73 (2005).
28. T.-Q. Nguyen, R. Martel, P. Avouris, M. L. Bushey, L. Brus, C. Nuckolls, Molecular interactions in one-dimensional organic nanostructures. *J. Am. Chem. Soc.* **126**, 5234–5242 (2004).
29. G. R. Desiraju, Cryptic crystallography. *Nat. Mater.* **1**, 77–79 (2002).
30. L. Kang, H. Fu, X. Cao, Q. Shi, J. Yao, Controlled morphogenesis of organic polyhedral nanocrystals from cubes, cubooctahedrons, to octahedrons by manipulating the growth kinetics. *J. Am. Chem. Soc.* **133**, 1895–1901 (2011).
31. S.-M. Lee, S.-N. Cho, J. Cheon, Anisotropic shape control of colloidal inorganic nanocrystals. *Adv. Mater.* **15**, 441–444 (2003).
32. S. X. M. Boerrigter, H. M. Cuppen, R. I. Ristic, J. N. Sherwood, P. Bennema, H. Meekes, Explanation for the supersaturation-dependent morphology of monoclinic paracetamol. *Cryst. Growth Des.* **2**, 357–361 (2002).
33. K. M. Morozov, P. Pander, L. G. Franca, A. V. Belonovski, E. I. Girshova, K. A. Ivanov, D. A. Livshits, N. V. Selenin, G. Pozina, A. P. Monkman, M. A. Kaliteevski, Opposite sign of polarization splitting in ultrastrongly coupled organic tamm plasmon structures. *J. Phys. Chem. C* **125**, 8376–8381 (2021).
34. C. Hosokawa, H. Tokailin, H. Higashi, T. Kusumoto, Efficient electroluminescence of distyrylarylene with hole transporting ability. *J. Appl. Phys.* **78**, 5831–5833 (1995).
35. B. Yin, J. Gu, M. Feng, G. C. Zhang, Z. Zhang, J. Zhong, C. Zhang, B. Wen, Y. S. Zhao, Epitaxial growth of dual-color-emitting organic heterostructures via binary solvent synergism driven sequential crystallization. *Nanoscale* **11**, 7111–7116 (2019).
36. X. Wang, Q. Liao, Z. Xu, Y. Wu, L. Wei, X. Lu, H. Fu, Exciton-polaritons with size-tunable coupling strengths in self-assembled organic microresonators. *ACS Photonics* **1**, 413–420 (2014).
37. H. Wang, B. Yue, Z. Xie, B. Gao, Y. Xu, L. Liu, H. Sun, Y. Ma, Controlled transition dipole alignment of energy donor and energy acceptor molecules in doped organic crystals, and the effect on intermolecular Förster energy transfer. *Phys. Chem. Chem. Phys.* **15**, 3527–3534 (2013).
38. C. A. M. Senevirathne, S. Yoshida, M. Auffray, M. Yahiro, B. S. B. Karunathilaka, F. Bencheikh, K. Goushi, A. S. D. Sandanayaka, T. Matsushima, C. Adachi, Recycling of triplets into singlets for high-performance organic lasers. *Adv. Opt. Mater.* **10**, 2101302 (2022).
39. J. Ren, Q. Liao, H. Huang, Y. Li, T. Gao, X. Ma, S. Schumacher, J. Yao, S. Bai, H. Fu, Efficient bosonic condensation of exciton polaritons in an H-aggregate organic single-crystal microcavity. *Nano Lett.* **20**, 7550–7557 (2020).
40. M. Lebental, J. S. Lauret, R. Hierle, J. Zyss, Highly directional stadium-shaped polymer microlasers. *Appl. Phys. Lett.* **88**, 031108 (2006).
41. S. Shinohara, T. Harayama, T. Fukushima, M. Hentschel, T. Sasaki, E. E. Narimanov, Chaos-assisted directional light emission from microcavity lasers. *Phys. Rev. Lett.* **104**, 163902 (2010).
42. Q. Song, W. Fang, B. Liu, S.-T. Ho, G. S. Solomon, H. Cao, Chaotic microcavity laser with high quality factor and unidirectional output. *Phys. Rev. A* **80**, 041807 (2009).
43. J. U. Nöckel, A. D. Stone, Ray and wave chaos in asymmetric resonant optical cavities. *Nature* **385**, 45–47 (1997).
44. S. Bittner, S. Guazzotti, Y. Zeng, X. Hu, H. Yılmaz, K. Kim, S. S. Oh, Q. J. Wang, O. Hess, H. Cao, Suppressing spatiotemporal lasing instabilities with wave-chaotic microcavities. *Science* **361**, 1225–1231 (2018).
45. X. Tang, L.-S. Cui, H.-C. Li, A. J. Gillett, F. Auras, Y.-K. Qu, C. Zhong, S. T. E. Jones, Z.-Q. Jiang, R. H. Friend, L.-S. Liao, Highly efficient luminescence from space-confined charge-transfer emitters. *Nat. Mater.* **19**, 1332–1338 (2020).
46. W. Liu, H. Yu, R. Hu, T. Xu, Y. Lun, J. Gan, S. Xu, Z. Yang, B. Z. Tang, Microlasers from AIE-active BODIPY derivative. *Small* **16**, 1907074 (2020).
47. F. Song, C. Zhang, H. Dong, Y. Fan, M.-Y. Wu, G. Shan, P. Lai, H. Gao, Y. S. Zhao, S. Chen, A switchable multimode microlaser based on an AIE microsphere. *J. Mater. Chem. C* **9**, 11180–11188 (2021).

Acknowledgments

Funding: This work was supported by the Natural Science Foundation of Hebei Province (no. B2020203013) and the Ministry of Science and Technology of China (no. 2018YFA0704802).

Author contributions: Conceptualization: Y.S.Z., J.G., and C.Z. Methodology: B.Y. Investigation: B.Y., J.L., J.H., H.W., and F.J.-S. Visualization: B.Y. Supervision: Y.S.Z., J.G., C.Z., and D.W. Writing—original draft: C.Z. and B.Y. Writing—review and editing: C.Z., J.G., B.Y., C.D., and H.J.
Competing interests: The authors declare that they have no competing interests. **Data and materials availability:** All data needed to evaluate the conclusions in the paper are present in the paper and/or the Supplementary Materials.

Submitted 23 March 2022
Accepted 1 September 2022
Published 21 October 2022
10.1126/sciadv.abn8106